

Structural and ferroelectric transitions in magnetic nickelate PbNiO_3

This content has been downloaded from IOPscience. Please scroll down to see the full text.

2014 *New J. Phys.* 16 015030

(<http://iopscience.iop.org/1367-2630/16/1/015030>)

View the [table of contents for this issue](#), or go to the [journal homepage](#) for more

Download details:

IP Address: 192.84.153.4

This content was downloaded on 03/02/2014 at 13:24

Please note that [terms and conditions apply](#).

New Journal of Physics

The open access journal at the forefront of physics

Deutsche Physikalische Gesellschaft  | IOP Institute of Physics

Structural and ferroelectric transitions in magnetic nickelate PbNiO_3

X F Hao^{1,2}, A Stroppa³, P Barone³, A Filippetti⁴, C Franchini²
and S Picozzi^{3,5}

¹ Institute of Applied Physics, Vienna University of Technology, Wiedner Hauptstrasse 8-10/134, 1040 Vienna, Austria

² Faculty of Physics, University of Vienna and Center for Computational Materials Science, A-1090 Wien, Austria

³ CNR-SPIN L'Aquila, Via Vetoio 10, I-67100 L'Aquila, Italy

⁴ CNR-IOM UOS Cagliari, c/o Dipartimento di Fisica, Università di Cagliari, Monserrato (CA), 09042 Italy

E-mail: silvia.picozzi@spin.cnr.it

Received 30 August 2013, revised 9 December 2013

Accepted for publication 12 December 2013

Published 30 January 2014

New Journal of Physics **16** (2014) 015030

[doi:10.1088/1367-2630/16/1/015030](https://doi.org/10.1088/1367-2630/16/1/015030)

Abstract

Density functional calculations have been tremendously useful in understanding the microscopic origin of multiferroicity and in quantifying relevant properties in many multiferroics and magnetoelectrics. Here, we focus on a relatively new and promising compound, PbNiO_3 . The structural, electronic and magnetic properties of its two polymorphs, i.e. the orthorhombic structure with space group *Pnma* and the rhombohedral LiNbO_3 -type structure with space group *R3c* have been studied by using density functional calculations within DFT+*U* and hybrid functional schemes. Our data convey an accurate description of the pressure-induced phase transition from the rhombohedral to orthorhombic phase at a predicted critical pressure of 5 GPa in agreement with the measured value of 3 GPa. Both phases show the G-type antiferromagnetic configuration as a magnetic ground state, but differ in the spatial anisotropy associated with nearest-neighbor exchange couplings, which is strongly weakened in the rhombohedral LiNbO_3 -type phase. The predicted large ferroelectric polarization of the rhombohedral phase (Hao *et al* 2012 *Phys. Rev. B* 014116) has been re-explored and analyzed in detail using partial density of states, Born effective

⁵ Author to whom any correspondence should be addressed.



Content from this work may be used under the terms of the [Creative Commons Attribution 3.0 licence](#).

Any further distribution of this work must maintain attribution to the author(s) and the title of the work, journal citation and DOI.

charge tensors, charge density difference, electron localization function analysis and distortion mode analysis. The asymmetric bonding between the Pb 6s and O 2p orbitals along the [111]-direction is responsible for the polar cationic displacement, giving rise to a predicted large ferroelectric polarization as high as $\sim 100 \mu\text{C cm}^{-2}$.

1. Introduction: a revised panorama on multiferroic compounds

Magnetic and ferroelectric materials are ubiquitous in modern science and present-day technology for their diverse applications, ranging from data storage to magnetic and ferroelectric random-access memories and spintronic devices [1–3]. Both ferromagnets and ferroelectrics are characterized by a spontaneous symmetry breaking that causes the appearance of a switchable long-range magnetic or dipolar ordering below a critical temperature, and they are commonly referred to as ferroics [4]. In recent years, the quest for (magnetoelectric) multifunctional integration within a single material has motivated a renewed interest in the class of so-called *multiferroic* materials, displaying the simultaneous presence of two or more spontaneous ferroic phases. The intrinsic combination of magnetism and ferroelectricity in this class of compounds could in principle allow for novel device paradigms exploiting their cross-coupled effect, e.g. allowing to control magnetization (polarization) by an external electric (magnetic) field. The intense research activity on this class of materials, both from the experimental and theoretical sides, is testified by the number of excellent review papers on the topic, opening promising prospects for applications also beyond the field of magnetic and ferroelectric materials, e.g. for information and energy harvesting technologies [5–10].

From the theoretical point of view, the intrinsically coupled and multifunctional nature of multiferroics poses numerous fundamental challenges. In fact, if on the one hand the theoretical understanding of magnetic insulators is rather well established, on the other hand a rigorous microscopic theory for ferroelectrics has been formulated only in the last few decades [11–13]. Naïvely, the difficulty arises from the fact that magnetic properties can be qualitatively traced back to well-defined localized quantities, i.e. the spin moments; conversely, electric dipoles in extended-state systems are well defined only in the very special case of a fully ionic material, while in general the electric polarization is a global property of the matter that cannot be decoupled in localized contributions, and is subject to change as a function of temperature. As a matter of fact, a rigorous definition of ferroelectric bulk polarization has been provided only in the early 90s via a quantum-mechanical approach based on Berry phases [11–13]. Furthermore, the microscopic origin of ferroelectricity is not unique, and the coexistence and interplay between structural distortions and electronic degrees of freedom (spin, charge, and orbital) has been proven to play a central role in the diverse mechanisms devised so far. In this respect, first-principles calculations based on the density-functional theory (DFT) have played an important role in the description, understanding as well as prediction—via identification of suitable material design rules—of magnetic, ferroelectric and magnetoelectric properties of multiferroics, due to its ability to describe the many active degrees of freedom within a comparable level of accuracy [3, 14–16].

Despite the advances reached in recent years, two major accomplishments still need to be fully achieved, namely (i) how to obtain an efficient coupling between ferroelectric

and magnetic orders in the multiferroic phase and (ii) how to realize a room-temperature multiferroic. The first issue is also directly related to a more fundamental question, which indeed lied at the origin of the renewed interest in multiferroics and still lacks a completely satisfactory answer: which conditions and constraints can determine the possibility to combine magnetism and ferroelectricity in a single homogenous material? For a long time it was thought that the two phenomena were mutually exclusive, and the formulation of an empirical exclusion rule claiming a chemical incompatibility between magnetism and ferroelectricity essentially slowed down the study of multiferroics by the 1970s. This exclusion rule was motivated by an early observation: most of the long-known (conventional) ferroelectrics are perovskite transition-metal oxides (BaTiO_3 , PbTiO_3 , KNbO_3 , and LiNbO_3), in which the polar distortion mainly involves an off-centering of the perovskite B-site transition-metal cation showing an empty d shell [17]. As rationalized later, the driving force behind the polar distortion in these conventional ferroelectrics comes from the tendency of empty d states to establish some degree of covalency with the surrounding oxygens [18–20]. On the other hand, magnetism requires partially filled d states to appear in perovskite oxides, thus apparently explaining the small overlap between the large families of ferroelectric and magnetic materials with the perovskite structure [21, 22]. A major breakthrough in the early 2000s was realizing that (i) the covalent bonding-mediated mechanism may not be the only possible origin of ferroelectricity and (ii) in some cases an electric polarization (called improper) may appear even if the polar displacement mode is not the only or the primary order parameter of the paraelectric–ferroelectric transition. A case in point is when a specific spin ordering breaks the inversion symmetry, thus causing the appearance of an improper ferroelectric phase with an intrinsically large magnetoelectric coupling. The latter phenomenon is observed in rare-earth manganites (TbMnO_3 and HoMnO_3) [8, 9]; unfortunately, these systems are usually frustrated (anti)ferromagnets, typically with rather low critical temperatures ($T_c \lesssim 40$ K). Furthermore, their frustrated magnetic configurations result in complex magnetoelectric effects (such as an electrical-induced swap of the spin-rotation planes in TbMnO_3) which may not be straightforwardly exploitable in applications.

It is well worth noting, however, that very recent theoretical advances pointed out that the aforementioned exclusion rule is less strict than expected even in the class of proper ferroelectric oxides. In fact, the conditions of multiferroicity in d^n perovskites have been recently derived from the pseudo Jahn–Teller effect, which considers ferroelectric displacements as triggered by vibronic coupling between ground and excited electronic states of opposite parity but same spin multiplicity [23]. According to this somewhat simplified approach, only some specific d^n and spin configurations allow for a coexistence of magnetism and ferroelectricity. A particularly interesting case is that of high-spin d^3 configuration, a situation realized in alkaline-earth manganites such as CaMnO_3 or SrMnO_3 ; these systems were shown to possess a weak ferroelectric instability mediated by a covalency-driven mechanism (such as in BaTiO_3), which at ambient conditions is hindered by other energetically favorable distortions, namely non-polar rotation/tiltings of BO_6 octahedra [24–26]. Applying strain or chemical pressure could in principle tune the balance between different structural instabilities, allowing for ferroelectricity to emerge, as indeed recently shown for strained CaMnO_3 films [27] and bulk $\text{Sr}_{1-x}\text{Ba}_x\text{MnO}_3$ [28]. Since both magnetic and ferroelectric instabilities are related to the same manganese B cations, the magnetoelectric coupling is expected to be strong in these systems [28–30], even though antiferromagnetic phases are apparently still favored; on the other hand, critical temperatures may be far larger than in frustrated magnets (e.g., $T_c \sim 185$ K

in $\text{Sr}_{0.5}\text{Ba}_{0.5}\text{MnO}_3$ [28]). Another prime example of the coupling between magnetism and ferroelectricity is represented by B-site magnetic ferroelectric perovskites such as MnMO_3 ($M = \text{Ti}, \text{Sn}$) in which the ferroelectric instabilities are driven by the chemical activity of the B-site atom [31].

Interesting theoretical advances were recently achieved noting that usually competing distortions in transition-metal perovskites, such as tilting/rotations of BO_6 octahedra, can in principle be tuned in order to trigger hybrid improper ferroelectricity [32, 33]. Such rotations in simple ABX_3 crystal structures generally preserve inversion symmetry, causing an ‘antiferroelectric’ ordering of A-site ions; these instabilities usually compete with covalency-driven B-site off-centerings, as it happens in e.g. CaTiO_3 or SrTiO_3 . However, several strategies have been proposed from a material design approach, which would allow the realization of ferroelectric systems arising from centric rotations, e.g. by layering perovskite blocks or by partial substitution of A-site ions [32, 34–42]. Interestingly, the magnetic properties may be also tuned and magnetoelectric effects are likely to appear, since rotations of corner-sharing octahedra buckle the inter-octahedral B–O–B angles which mediate the interplay of electronic and magnetic degrees of freedom. As an example, a theoretical calculation has shown that a linear magnetoelectric effect, allowing for electric-field control of magnetization, is predicted to appear in a layered $\text{Ca}_3\text{Mn}_2\text{O}_7$ [37]. Due to the generally high temperatures at which these non-polar distortions are expected to appear, as compared to frustrated magnetic phases, in the near future the proposed approach could lead to the identification of new multiferroic materials at room temperature. Another possibility is to explicitly dope with magnetic dopants (e.g. Ti–V substitution) the layered $\text{La}_3\text{Ti}_2\text{O}_7$ structure [39, 40] which in itself displays robust ferroelectricity due to the breaking of the octahedral rotation pattern in the direction parallel to the stacking [38]. Furthermore, other typical distortions in perovskites, such as non-polar Jahn–Teller ones, can in principle play a role in the appearance of both hybrid improper ferroelectricity and magnetoelectric coupling, as recently shown in a new class of materials, namely metal–organic frameworks with perovskite geometry [43, 44]. As opposed to their inorganic counterparts, metal–organic frameworks offer the possibility of varying their additional degrees of freedom, arising from organic/inorganic duality, which could be exploited for a rational design of new materials with enhanced functionalities.

With respect to the issue of having a room-temperature multiferroic, finally, at the moment the most efficient mechanism in oxide perovskites is that realized in A-site driven ferroelectrics such as BiFeO_3 (and possibly BiMnO_3 and PbVO_3), where the presence of lone pairs in Bi^{3+} or Pb^{2+} plays a central role in the origin of ferroelectric polarization.

Such a mechanism, first theoretically proposed for BiMnO_3 [45] and then experimentally verified in the widely investigated BiFeO_3 [46–49], originates from the on-site sp rehybridization of the two 6s electrons of bismuth or lead that do not participate in chemical bonds, thus showing a high polarizability which results in a very large ferroelectric polarization ($\sim 100 \mu\text{C cm}^{-2}$ [50] in BiFeO_3). On the other hand, magnetism is guaranteed by the B-site magnetic Fe^{3+} (d^5) ions. Due to the independent origin of ferroelectricity and magnetism in this type of multiferroics, the magnetoelectric coupling has been long thought to be rather small; however, a number of recent observations indicate that magnetoelectric effects in BiFeO_3 can be significant, suggesting also an important role played by the large ferroelectric polarization in modulating the magnetic ordering [51–54]. These recent findings suggest potential relevance also in this class of proper multiferroics, where the inherently giant ferroelectric polarization together with unusual magnetoelectric effects can find interesting technological applications.

It should be noted, however, that the ferroelectric nature of BiMnO_3 has been the subject of controversial studies. After the initial claim of lone-pair ferroelectricity [45], computational structural optimizations revealed that the ferroelectric phase is not stable and indeed converges to the centrosymmetric $C2/c$ structure [55]. This result was later confirmed by the experimental structural data of Belik *et al* [56]. Subsequent studies tried to reconcile these two seemingly conflicting pictures by proposing that, even considering a centrosymmetric crystal structure, BiMnO_3 can behave as an improper ferroelectric (i.e. where ferroelectricity is induced by the magnetic order, which breaks the inversion symmetry) [57]. Moreover, Solovyev and Pchelkina [57] suggests that BiMnO_3 should be a rare example of materials, where ferroelectricity indeed coexists with (canted) ferromagnetism, and demonstrates how the polarization can be controlled by the magnetic field.

In this latter context of A -site-driven ferroelectrics with large polarization, we can place a relatively new multiferroic, PbNiO_3 , which has recently attracted much interest and which will be the focus of the remaining part of the paper. By means of density-functional simulations, complemented by state-of-the-art hybrid functionals and DFT+ U approaches, we have explored the structural, electronic and magnetic properties of two different phases of PbNiO_3 , i.e. the orthorhombic and the LiNbO_3 -like rhombohedral polymorphs. The outcomes of our simulations allow for a thorough understanding of the PbNiO_3 electronic structure, in turn leading to a microscopic understanding of the origin of its ferroelectric polarization, pressure-induced phase transition and magnetism, thereby constituting an additional example of how *ab initio* simulations can be useful in the framework of new multiferroics.

2. Prediction of multiferroicity in the new compound PbNiO_3

2.1. Introduction

The perovskite structure is ubiquitous in materials science, especially among oxide materials. They show very different properties, like superconductivity, colossal magnetoresistance, ionic conductivity and dielectric properties, which are of great importance in numerous technological applications [58, 59]. The perovskite structure, with general formula ABX_3 , gives the possibility to accommodate a large variety of A and B cations with different $A-X$ and $B-X$ bond lengths. Due to this great flexibility, it is possible to realize different types of distortions from the ideal cubic structure. These include tilting of the octahedra, off-centering displacements of the cations out of the coordination polyhedra, and deformations of the octahedra driven by electronic factors (i.e. Jahn–Teller distortions) [23, 60, 61]. The electronic, magnetic and dielectric properties of perovskites depend crucially on the details of these distortions [58, 59]. A useful structural related parameter, the so-called Goldschmidt tolerance factor t , can be used to predict the possible low-symmetry structural distortion, starting from the ideal ABX_3 cubic structure. It is defined as

$$t = \frac{r_A + r_O}{\sqrt{2}(r_B + r_O)}, \quad (1)$$

where r_A , r_B and r_O denote the ionic radii of A , B and oxygen, respectively [62]. A range of t values approximately between 0.9 and 1.0 corresponds to stable cubic perovskite structures. For $t > 1$, the equilibrium structure shows face sharing of BO_6 octahedra, resulting in hexagonal perovskites. On the other hand, for $t < 0.9$ cooperative rotations of the octahedra yield lower symmetry perovskites such as tetragonal, orthorhombic, rhombohedral, etc [62].

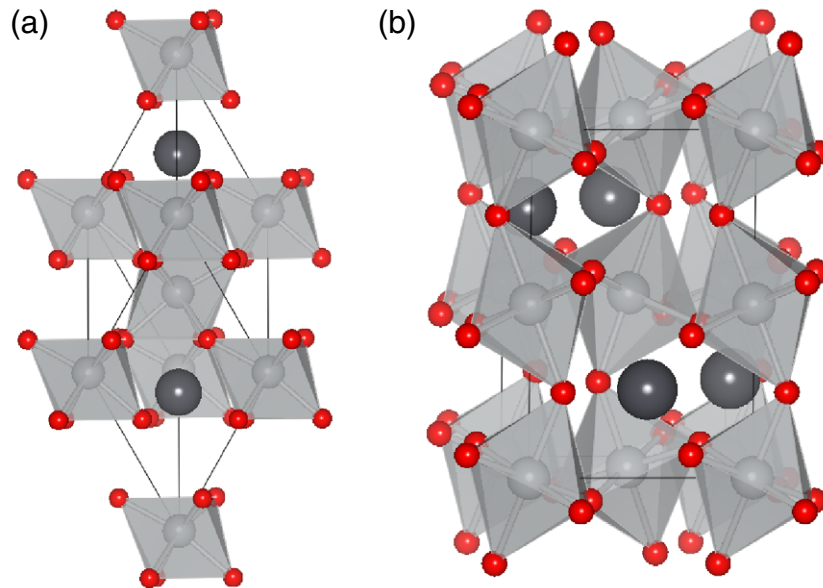


Figure 1. Crystal structures for rhombohedral (LiNbO₃-type) (a) and orthorhombic (b) PbNiO₃, the black (large), gray (medium) and red (small) spheres denote Pb, Ni and O atoms, respectively.

External perturbations, like temperature and/or pressure, can be used to induce phase transitions giving access to other metastable phases. The change of octahedral distortions have been observed in many perovskite-related systems upon heating or cooling, and application of pressure and alloying (i.e. chemical pressure). For example, recently Inaguma *et al* have successfully synthesized two polymorphs of PbNiO₃ and CdPbO₃, the orthorhombic (space group *Pnma*) and the LiNbO₃-type rhombohedral structure (space group *R3c*), both shown in figure 1. *In situ* energy dispersive x-ray diffraction experiments revealed that a phase transition between the two phases could be realized irreversibly in PbNiO₃ if the appropriate thermodynamic conditions, 400 °C and 3 GPa are established [63]. The structural phase transition in CdPbO₃ strongly depends on heating temperature and there are temperature ranges in which both phases are seen to coexist [64]. Additionally, Goldschmit diagram analysis [63, 64] suggests a boundary between the orthorhombic and rhombohedral phase in the vicinity of $t = 0.85$. On the basis of this argument, it has been predicted that several compounds could be stabilized in both phases under different pressure conditions [64]. Both phases show interesting electronic and magnetic properties [63–66]. The magnetic susceptibility measurements showed that the orthorhombic and rhombohedral phases in PbNiO₃ undergo an antiferromagnetic transition at 225 and 205 K, respectively. In addition, both phases have semiconducting behavior. Bond valence sum based on the refined structures and XPS data revealed that the valence state in both phases should be Pb⁴⁺Ni²⁺O₃ [63], but DFT-based calculations have clarified that this formal valence view is perturbed by the strong Pb 6s-O 2p hybridization which in turn results in enhanced ferroelectric instabilities [65]. Of particular interest is that the non-centrosymmetric rhombohedral structure allows a relative displacement of Pb, Ni and O atoms along the threefold [111]-axis, i.e. out of the centers of their coordination polyhedra, thus inducing a spontaneous polarization, which put forward the LiNbO₃-type PbNiO₃ as a potential candidate for proper multiferroic behavior near room temperature.

2.2. Methods

We performed first-principles calculations using the Vienna *ab initio* Simulation Package (VASP) [67]. All the results were obtained using the projector-augmented plane-wave method [68] by explicitly treating 14 valence electrons for Pb ($5d^{10}6s^26p^2$), 10 for Ni ($3d^84s^2$) and 6 for oxygen ($2s^22p^4$). Spin-orbit coupling was not included. Brillouin zone integrations were performed using a Gaussian broadening [69] of 0.1 eV during all relaxations, and the ions were relaxed until the Hellmann–Feynman forces were less than 10^{-2} eV Å $^{-1}$. We used a $8 \times 6 \times 8$ and $8 \times 8 \times 8$ Monkhorst–Pack [70] k -point mesh centered at Γ for orthorhombic and rhombohedral PbNiO₃, respectively. We used a large basis set defined by plane-wave cutoff of 600 eV. These values ensure good convergence for all the investigated properties.

It is well known that local and semi-local density functionals (generalized gradient approximation (GGA)) [71] usually underestimate the size of the band gap in ‘strongly’ correlated systems, e.g. those containing localized d orbitals, and they even incorrectly predict metallic behavior for materials that are known to be insulators. Therefore, in order to deal with these shortcomings, we used the GGA+ U method [72, 73] where the strong Coulomb repulsion between localized d states is treated by adding a Hubbard-like term to the effective potential. This usually gives an improved description of correlation effects in magnetic transition-metal oxides [74–77]. The GGA+ U method requires two parameters, the Hubbard parameter U and the exchange interaction J . In this work, we adopted the rotationally invariant approach in which the parameters U and J do not enter separately, but rather as an effective Hubbard parameter given by their difference ($U_{\text{eff}} = U - J$) [78, 79]. The on-site correction was set to be 4.6 eV for Ni²⁺ 3d electrons adapted from previous self-consistent calculations [74]. However, we tested that the results are not strongly dependent on the choice of the U_{eff} parameter chosen within a reasonable range of U values. As a further check we have also applied the Heyd–Scuseria–Ernzerhof (HSE) screened hybrid functional [80]. In the HSE method the short-range (sr) part of the exchange interaction (X) is constructed by a mixing of exact non-local Hartree–Fock exchange and approximated semi-local Perdew–Burke–Ernzerhof (PBE) exchange. The remaining contributions to the exchange-correlation energy, namely the long-range (lr) exchange interaction and the electronic correlation (C), are treated at the PBE level only, as defined in the following:

$$E_{XC}^{\text{HSE}} = \alpha E_X^{\text{HF,sr},\mu} + (1 - \alpha) E_X^{\text{PBE,sr},\mu} + E_X^{\text{PBE,lr},\mu} + E_C^{\text{PBE}}. \quad (2)$$

The partitioning between sr and lr interactions is achieved by properly decomposing the Coulomb kernel ($1/r$, with $r = |\mathbf{r} - \mathbf{r}'|$) through the characteristic parameter μ , which controls the range separation between the short (S) and long (L) range part

$$\frac{1}{r} = S_\mu(r) + L_\mu(r) = \frac{\text{erfc}(\mu r)}{r} + \frac{\text{erf}(\mu r)}{r}. \quad (3)$$

We have used here $\mu = 0.20$ Å $^{-1}$ and $\alpha = 0.25$, which is known to provide a very accurate description of the structural properties of PbNiO₃ [65]. A more detailed discussion of the role of α on the ground state properties of magnetic oxide perovskites can be found in [81]. In the last few years, the application of hybrid functionals to a wide class of solid state systems, including ferroelectrics [82–84], multiferroics [16, 65, 66] and magnetic perovskites [81, 85] has shown that an improved description of ground state structural, electronic and magnetic properties with respect to the standard GGA and GGA+ U can be achieved, in general.

Table 1. Structural parameters for LiNbO₃-type PbNiO₃ within GGA, GGA+*U* and HSE methods, compared with the available experimental data. *a*, *c* are the lattice parameters in the hexagonal setting, whereas *x*, *y*, and *z* are the internal atomic positions of Pb and O. Ni ions sit in the (6*a*) (0,0,0) positions. Bond lengths of Pb–O and Ni–O are also reported. $\widehat{\text{Ni–O–Ni}}$ (°) is the Ni–O–Ni angle.

	GGA	GGA+ <i>U</i>	HSE	Expt.
<i>a</i> (Å)	5.442	5.430	5.359	5.363
<i>c</i> (Å)	13.737	14.353	14.209	14.090
<i>z</i> _{Pb}	0.2226	0.2885	0.2898	0.2864
<i>x</i> _O	0.0605	0.0532	0.0468	0.0487
<i>y</i> _O	0.2598	0.3543	0.3579	0.3657
<i>z</i> _O	0.0931	0.0702	0.0687	0.0668
Ni–O (Å)	2.051 1.905	2.128 2.060	2.119 2.053	2.109 2.071
Pb–O (Å)	2.395 2.238	2.310 2.174	2.258 2.121	2.246 2.104
$\widehat{\text{Ni–O–Ni}}$ (°)	147.8	140.6	138.1	136.7

Due to the high computational cost of HSE calculations, the Fock exchange was sampled using the twofold reduced \mathbf{k} -point grid.

Phonon dispersions were calculated within the density functional perturbation theory using the code PHONOPY [86].

In order to determine the magnetic ground state, we considered ferromagnetic, A-type, C-type as well as G-type antiferromagnetic orderings. The calculations show that the G-type configuration is the magnetic ground state for both the systems considered hereafter. Therefore, we will focus on the G-type ordering from now on, unless otherwise specified.

2.3. Results and discussion

2.3.1. Equilibrium structures and phase stability. As reported in our previous work [65], the GGA+*U* and HSE schemes are essential to reproduce the structural properties of rhombohedral PbNiO₃: the HSE and, to a lesser extent, GGA+*U* reproduce the structural properties in good agreement with experiments, while the GGA fails to do so. The collection of the structural data for the LiNbO₃-type rhombohedral phase is proposed again in table 1.

Results for the high pressure orthorhombic phase are shown in table 2. The GGA functional could not reproduce the atomic positions accurately, giving rise to incorrect bond lengths and angles, although there seems to be good agreement for the lattice parameters. The inclusion of either the on-site *U* or the Fock exchange improves the GGA description.

To explore the phase stability, the structures were fully relaxed for all volumes using force as well as stress minimization within GGA and GGA+*U* methods. The total energy versus volume is shown in figure 2. Note that the GGA method (figure 2(a)) predicts the orthorhombic *Pnma* phase as the ground-state structure for PbNiO₃, which is in contrast with experiments [63]. On the other hand, GGA+*U* (figures 2(b), (c)) predicts the rhombohedral *R3c* phase as the ground state for PbNiO₃ although with a slightly larger volume, and correctly describes the relative stability of these two phases: the predicted GGA+*U* transition pressure

Table 2. Structural parameters for orthorhombic PbNiO_3 via GGA, GGA+ U and HSE methods, compared with the available experimental data. a , b and c denote the lattice parameters in the orthorhombic setting. Pb ($4c$) and O ($4c$ and $8d$) Wyckoff positions are reported. Ni is in the ($4a$) ($0,0,0$) position (not included in the table). Bond lengths of Pb–O and Ni–O are given. $\widehat{\text{Ni–O–Ni}}$ ($^\circ$) is the Ni–O–Ni angle.

	GGA	GGA+ U	HSE	Expt.
a (\AA)	5.542	5.484	5.392	5.463 25
b (\AA)	7.693	8.062	8.052	7.707 41
c (\AA)	5.370	5.278	5.193	5.358 27
v ($\text{\AA}^3/\text{unit cell}$)	228.95	233.35	225.46	225.62
x_{Pb}	0.4464	0.4406	0.4382	0.458 29
z_{Pb}	0.0151	0.0311	0.0339	0.007 61
$x_{\text{O}4c}$	0.5405	0.5623	0.5720	0.593
$z_{\text{O}4c}$	0.6001	0.6323	0.6403	0.6236
$x_{\text{O}8d}$	0.2024	0.2027	0.2003	0.1846
$y_{\text{O}8d}$	0.0529	0.0728	0.0785	0.0748
$z_{\text{O}8d}$	0.3000	0.2995	0.3015	0.3192
Ni–O _{4c} (\AA)	2.009	2.160	2.176	2.100
Ni–O _{8d} (\AA)	2.009	2.031	2.018	2.068
	2.005	2.020	2.004	2.059
Pb–O _{4c} (\AA)	2.333	2.247	2.172	2.185
	2.289	2.208	2.167	2.116
Pb–O _{8d} (\AA)	2.729	2.981	3.001	2.810
	2.543	2.398	2.342	2.617
	2.302	2.215	2.153	2.053
$\widehat{\text{Ni–O}_{4c}\text{–Ni}}$ ($^\circ$)	146.3	137.8	135.4	133.1
$\widehat{\text{Ni–O}_{8d}\text{–Ni}}$ ($^\circ$)	147.9	140.0	137.0	136.0

is $P \approx 5 \text{ GPa}$, slightly larger than the experimental value, $\approx 3 \text{ GPa}$ [63] (the deviation can be caused by temperature effects, which are not taken into account in the present work), whereas the calculated volume collapse, $\approx 4.5\%$, is in agreement with the reported measured value of $\approx 3.5\%$.

To investigate the possible role of phonon instabilities in the observed structural transition from the low pressure $R3c$ phase to the high pressure $Pnma$ phase, we have computed the phonon spectra of both structures at their equilibrium volume ($V_{R3c} = 244.32 \text{ \AA}^3$, $V_{Pnma} = 233.39 \text{ \AA}^3$) as well as at compressed ($R3c$, $V = 244 \text{ \AA}^3$) and expanded ($Pnma$, $V = 250 \text{ \AA}^3$) volumes. The results shown in figure 3 indicate that none of the considered phases exhibit negative modes in the off-equilibrium regime, suggesting that the pressure-induced structural transition is not phonon-mediated, but rather connected with electronic modifications of the chemical bonds. This implies that the $R3c/Pnma$ phases are metastable structures at high/low pressures. Due to the high computational workload and the good performance of the GGA+ U method, we did not perform a similar study with the HSE approach.

2.3.2. The orthorhombic ($Pnma$) phase. As previously stated, the G-type antiferromagnetic configuration, where each Ni ion is surrounded by six nearest-neighbor Ni ions with the

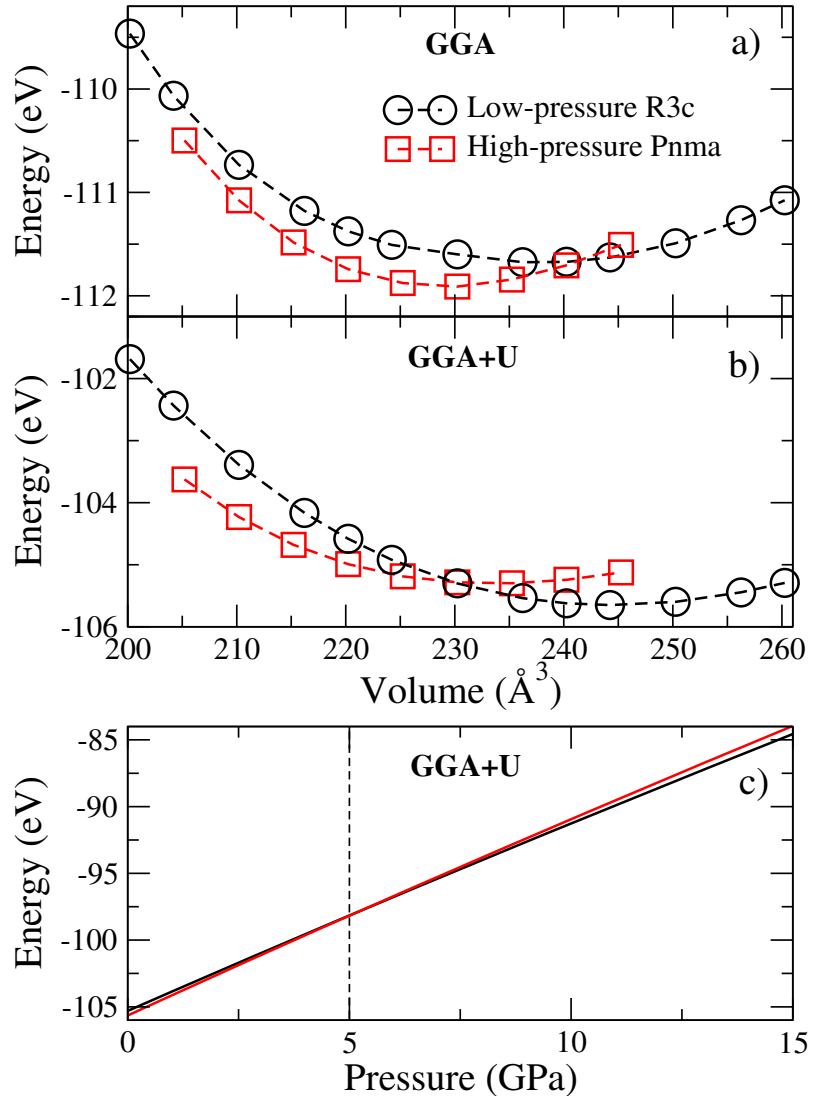


Figure 2. (a, b) Calculated total energy versus cell volume per unit cell for G-type PbNiO_3 in the rhombohedral $R\bar{3}c$ and the orthorhombic $Pnma$ phase as obtained by GGA (a) and GGA+ U (b). (c) Enthalpy versus pressure curve (GGA+ U). The vertical dashed line indicates the critical pressure at which the transition occurs.

opposite spin direction, is the most stable configuration, with an energy gain with respect to ferromagnetic, C-type antiferromagnetic and A-type antiferromagnetic configurations of 55.7, 25.6 and 32.7 meV per formula unit, respectively. By mapping these energies onto a Heisenberg model Hamiltonian $H = \frac{1}{2} \sum_{ij} J_{ij} S_i S_j$ with normalized spins, we can estimate the nearest-neighbor exchange couplings J_{\parallel} and J_{\perp} , parallel and perpendicular to the ac -plane, respectively, as well as the next-nearest neighbor isotropic (additional—and expected to be smaller—anisotropy of possible next-nearest neighbor interactions has been neglected) exchange coupling J_2 . We find a significant anisotropy of nearest-neighbor exchange couplings, namely $J_{\parallel} = 7.85$ meV and $J_{\perp} = 12.15$ meV, that can be most probably ascribed to the different buckling of Ni–O–Ni angles (by $\approx 3^\circ$) mediating the superexchange interaction between neighboring Ni ions. Furthermore, the next-nearest-neighbor exchange interaction is predicted

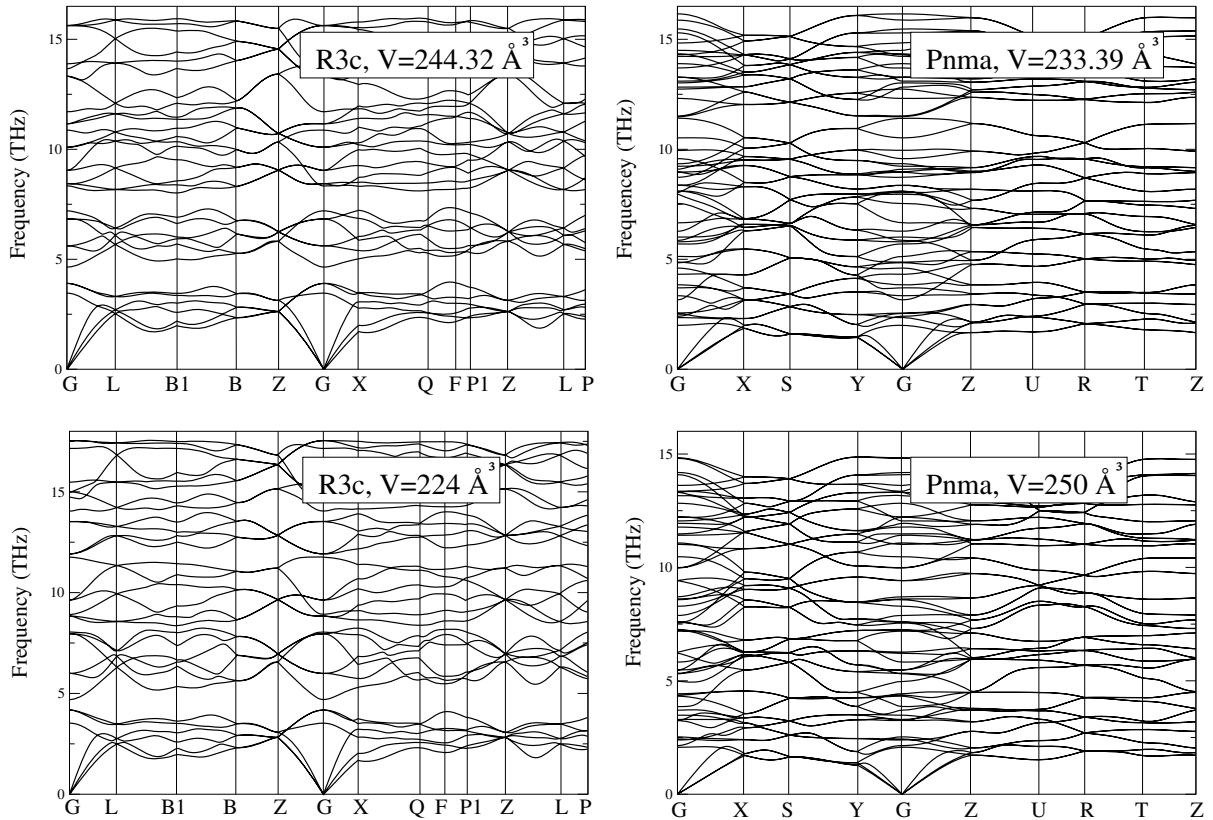


Figure 3. Calculated (GGA+U) phonon spectra for the *R3c* and *Pnma* phases at their equilibrium (top) and off-equilibrium (bottom) volume. The relative stability of the *R3c* and *Pnma* phases with respect to the volume is given in figure 2.

to be weakly ferromagnetic, $J_2 = -0.16$ meV. The critical temperature for the magnetic transition can be then predicted in a mean-field approach as $T_c \sim \frac{2}{3}(2J_{\parallel} + J_{\perp} - 6J_2)$, which gives $T_c \sim 223$ K, in perfect but perhaps fortuitous agreement with the experimental value $T_c = 225$ K. Indeed, the mean-field value is known to overestimate the exact solution. A more accurate classical Monte Carlo calculation on a $20 \times 20 \times 20$ cell, using a Metropolis algorithm, predicts $T_c = 186$ K, which is 20% lower than the experimental value, well within the typical error associated with *ab initio* predictions of critical temperatures [87]. Such underestimation is most probably due to the artifacts of the GGA+U approach [88].

With respect to the electronic properties of the orthorhombic phase, an interesting issue is related to the possible existence of lone-pairs on Pb ions. In order to evaluate the nominal oxidation state of the atoms, a valence bond sum based on the Rietveld structural refinement as well as XPS measurements were used [63], suggesting that the ionic configuration of PbNiO_3 is Pb^{4+} , Ni^{2+} , and O^{2-} . The orthorhombic PbNiO_3 was then reported as the first example of the perovskite containing a tetravalent A-site cation without lone pair electrons [63].

To gain more insights into the valence state in orthorhombic PbNiO_3 , the calculated total and partial density of states for G-type configuration within the corresponding optimized structure via GGA+U and HSE schemes are given in figure 4. The top of the valence band is set to zero, as indicated by a dotted vertical line. Note that the electronic structure obtained within GGA+U and HSE is very similar. The band centered at -7 eV is dominated by the Pb 6s orbital.

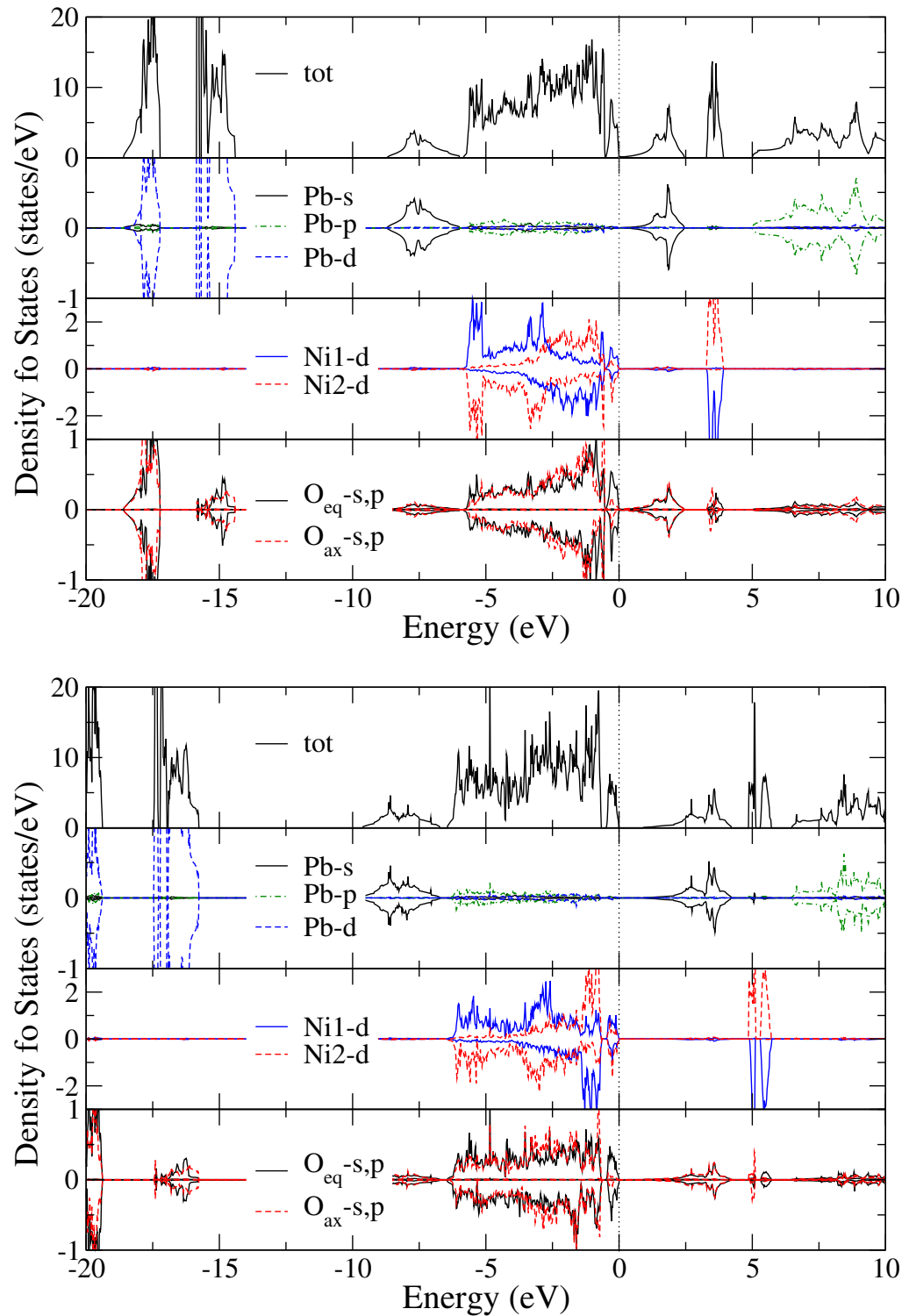


Figure 4. Calculated total and partial density of states for G-type antiferromagnetic configuration of orthorhombic PbNiO_3 by using GGA+ U (up) and HSE (down) schemes within the corresponding optimized structure, respectively.

An energy overlap between the Pb 6s and O 2p orbitals suggests a covalent bond between them. The Ni 3d states are located starting at -6 eV to the Fermi level. The energy overlap of the Ni 3d and O 2p states in the whole valence band indicates the presence of a strong covalent bonding between these two ions. The electronic configuration of Ni ions is $t_{2g}^6 e_g^2$, as can be deduced from the total occupation of the t_{2g} states in both spin channels and of the e_g states in one spin-channel, and empty e_g states in the other spin channel. This results in 2+ state of Ni atom and $1.66\mu_B$ magnetic moment, very close to the nominal d^8 states. However, the valence state for the Pb ion cannot be determined easily. As shown before for the rhombohedral $R3c$ phase [65], the significant hybridization between Pb 6s and O 2p orbitals suggests a reduction of the O valence state, i.e., the valence state of the Pb ion is smaller than the nominal 4+. Our analysis indicates that the simple concept of nominal valence charge is not sufficient to capture the subtle electronic properties of this system.

According to the density of states shown in the upper panel of figure 4, the GGA+ U calculation results in a semiconducting behavior with a narrow band gap of 0.05 eV , which does not depend much on the chosen U . This is not unexpected since the band gap is between the bottom of Pb 6s conduction band and the top of O 2p valence states, which are states not affected by the Hubbard term.

Although the electronic structure obtained via GGA+ U and HSE method are very similar, some differences can be found. In HSE, the spectral distribution of O 2s and Pb 5d states are shifted considerably downwards. Also, the bonding Pb 6s states are shifted downwards, while the antibonding states are shifted upwards, increasing the band gap to 1.05 eV , which is much larger than that of GGA+ U . It has been argued that the downward shift of d states in transition-metal oxides is an artifact of the LDA+ U scheme [88].

2.3.3. The rhombohedral LiNbO_3 -type phase. The low-pressure phase of PbNiO_3 has a rhombohedrally non-centrosymmetric structure with the $R3c$ space group, which is isostructural with the most common multiferroic material BiFeO_3 [89]. More interestingly, the rhombohedral phase undergoes antiferromagnetic transition at 205 K , and exhibits semiconducting transport properties [63]. This therefore suggests a possible multiferroic behavior, i.e. co-existence of ferroelectric and magnetic properties. From the energy differences between the considered ferromagnetic, C-type and A-type configurations with respect to the G-type antiferromagnetic ground state, we could estimate the relevant exchange coupling constants $J_1 = 8.69\text{ meV}$, $J_2 = 0.27\text{ meV}$ and $J_3 = 0.19\text{ meV}$ (where J_3 represents now the isotropic exchange interaction between the third nearest neighboring Ni ions). The nearest-neighbor exchange interactions are now isotropic, consistently with the $R3c$ symmetry of the rhombohedral structure. A small anisotropy could in principle be present in the next nearest neighbor exchange interactions, which is however unattainable with the considered magnetic configurations. More interestingly, however, the next nearest neighbor interaction J_2 is found to be weakly antiferromagnetic, implying a weak magnetic frustration that can well explain the lower critical temperature as compared to the orthorhombic phase. From our estimated J_{ij} , the mean-field formula predicts $T_c \sim 195\text{ K}$ (the MonteCarlo approach gives 143 K). Again, the predicted T_c significantly underestimates the experimental value; however, the trend we find, i.e. the lowering of the magnetic Néel temperature upon structural transition, is in qualitative agreement with experimental observations, being related to both the weak magnetic frustration introduced by the antiferromagnetic J_2 as well as to a volume effect (responsible for a slight decrease of the nearest-neighbor exchange interaction).

Table 3. Ferroelectric polarization of rhombohedral PbNiO_3 along the [111]-direction, using GGA+ U ($U_{\text{eff}} = 7.6 \text{ eV}$) and HSE schemes. Point charge model (PCM) estimate is also given for comparison. HSE(GGA+ U) means a HSE calculation at fixed GGA+ U geometry for the ferroelectric as well as for the paraelectric structure. The partial ionic and electronic contributions are also given. Units are in $\mu\text{C cm}^{-2}$.

	\mathbf{P}_{ion}	\mathbf{P}_{ele}	\mathbf{P}_{tot}	\mathbf{P}_{PCM}
GGA+ U	113.7	-18.0	95.7	87.6
HSE	114.0	-14.5	99.5	95.5
HSE(GGA+ U)	113.7	-20.5	93.3	87.6

In the next section, we will mainly focus on the ferroelectric properties of rhombohedral PbNiO_3 and the apparently mysterious origin of a strong polarization induced by a nominally Pb^{4+} ion.

2.3.4. Ferroelectric properties. We evaluated the spontaneous polarization \mathbf{P} of rhombohedral PbNiO_3 from first principles considering as centrosymmetric structural reference the $R\text{-}3c$ symmetry, and we linearly interpolate the atomic positions between the centric and the polar phase, i.e. the so-called adiabatic path [11–13].

For the paraelectric phase, we used the same lattice constant and rhombohedral angle of the ferroelectric one, but we relaxed the internal atomic positions. It is worth mentioning that the GGA+ U calculations were carried out with $U_{\text{eff}} = 7.6 \text{ eV}$ using the relaxed structure obtained by $U_{\text{eff}} = 4.6 \text{ eV}$, since this value gives an insulating ground state for both polar and non-polar systems.

In general, it is useful to represent the spontaneous polarization \mathbf{P}_{tot} as a sum of the ionic contribution, \mathbf{P}_{ion} , and the electronic, \mathbf{P}_{ele} : $\mathbf{P}_{\text{tot}} = \mathbf{P}_{\text{ion}} + \mathbf{P}_{\text{ele}}$ [90]. Although the ionic and electronic components are sometimes useful tools for qualitative discussions, one has to keep in mind that only the total polarization difference between two structural configurations has a physical meaning [15]. In table 3, we report the ionic and electronic contributions to the difference of ferroelectric polarization between the polar and non-polar configuration, both at GGA+ U and HSE level. The computed total polarization \mathbf{P}_{tot} reaches 95.7 and $99.5 \mu\text{C cm}^{-2}$ at GGA+ U and HSE level, respectively, comparable to that of BiFeO_3 [16, 46]. The spontaneous polarization of LiNbO_3 and ZnSnO_3 was reported to be $80 \mu\text{C cm}^{-2}$ [91] and $56.9 \mu\text{C cm}^{-2}$ [92], respectively, which is much smaller than the present results for rhombohedral PbNiO_3 . As far as the relative stability is concerned, the energy barrier between the centric and the polar phase is $\sim 0.55 \text{ eV}$ per formula unit for DFT+ U and HSE, thus supporting the thermodynamic stability of the polar $R3c$ phase with respect to the centrosymmetric $R\text{-}3c$ phase, and indicating that the LiNbO_3 -type PbNiO_3 may be ferroelectric with a relatively high Curie temperature.

In order to separate purely electronic and structural effects on the calculation of the polarization, we performed the HSE calculations using the GGA+ U geometry, which we denote as $\mathbf{P}_{\text{tot}}^{\text{HSE(GGA+}U)}$. Note that the ionic contribution is of course the same in both cases, while $\mathbf{P}_{\text{tot}}^{\text{GGA+}U} = 95.7 \mu\text{C cm}^{-2}$ and $\mathbf{P}_{\text{tot}}^{\text{HSE(GGA+}U)} = 93.3 \mu\text{C cm}^{-2}$. Therefore, keeping the volume unchanged and including the Fock exchange, the polarization decreases, while the band gap

Table 4. Born effective charge tensors for Pb and Ni in PbNiO_3 (with ferroelectric and paraelectric phases) via linear-response formalism within the GGA+ U ($U_{\text{eff}} = 7.6 \text{ eV}$) method.

	Ferroelectric			Paraelectric	
Pb	4.32	0.87	0.00	4.43	0.00
	-0.87	4.32	0.00	0.00	4.43
	0.00	0.00	4.57	0.00	0.00
Ni	2.00	0.45	0.00	2.00	0.71
	-0.45	2.00	0.00	-0.71	2.00
	0.00	0.00	1.92	0.00	0.00
					1.91

increases from 0.37 eV (GGA+ U) to 0.89 eV (HSE). This scenario agrees with the intuitive expectation that the larger the energy gap, the lower the polarization should be [16].

Additionally, it is sometimes useful to evaluate the polarization within the PCM. It is evaluated using the following equation

$$P_{\text{PCM}} = \frac{e}{\Omega} \sum_i Z_i^v \vec{\Delta r}_i, \quad (4)$$

where Ω , Z_i^v and $\vec{\Delta r}_i$ denote the unit-cell volume, the formal charge and the displacement of the ion i , respectively. A large difference between the PCM value and the \mathbf{P}_{tot} obtained from a fully quantum mechanical calculation signals that covalency effects are at play. Our PCM polarization value is $87.6 \mu\text{C cm}^{-2}$ and $95.5 \mu\text{C cm}^{-2}$ for GGA+ U and HSE atomic structures, respectively. The closeness of HSE-structure PCM and full HSE values of polarization indicates that (i) the HSE description of PbNiO_3 is more ionic than that of GGA+ U (equivalently, we can say that nominal and effective atomic charges are similar in HSE); (ii) LiNbO₃-type PbNiO_3 should be a proper displacive ferroelectric. Note that even in the absence of highly anomalous charges, covalent effects can play an appreciable role in the determination of large polar $\vec{\Delta r}_i$ displacements.

Density of states analysis. The comparison of the density of states between ferroelectric $R3c$ and paraelectric $R-3c$ phase [65] indicates that the major variation is the $\sim 2 \text{ eV}$ downshift and the broadening of the Pb 6s–O 2p spectral weight from the paraelectric to the ferroelectric phase. This highlights the role of the Pb 6s–O 2p hybridization in stabilizing the non-centric ferroelectric phase. A similar broadening of the bonding Pb 6s–O 2p states was found in BiFeO_3 [46, 93] where the stereochemical activity of the 6s lone pair of Bi ions is the driving force for the off-centering distortions.

Born effective charge analysis. We have calculated Born effective charge tensors using the linear-response formalism within GGA+ U ($U_{\text{eff}} = 7.6 \text{ eV}$). Table 4 lists the Born effective charge tensors of Pb and Ni in PbNiO_3 in the ferroelectric and paraelectric phases. For Pb it was shown in [65] that its static charge (2.15) is much smaller than the nominal 4+; on the other hand, its Born effective charge is much larger than the static charge, indicating the presence of a large anomalous contribution due to covalent bonding between Pb and O ions. This situation is analogous to that of the highly polarized BiFeO_3 [46, 93].

Note also the larger zz component of Pb effective charge that can be traced back to the anisotropy of bond lengths in the PbO_6 octahedra in the ferroelectric phase, and indicates that

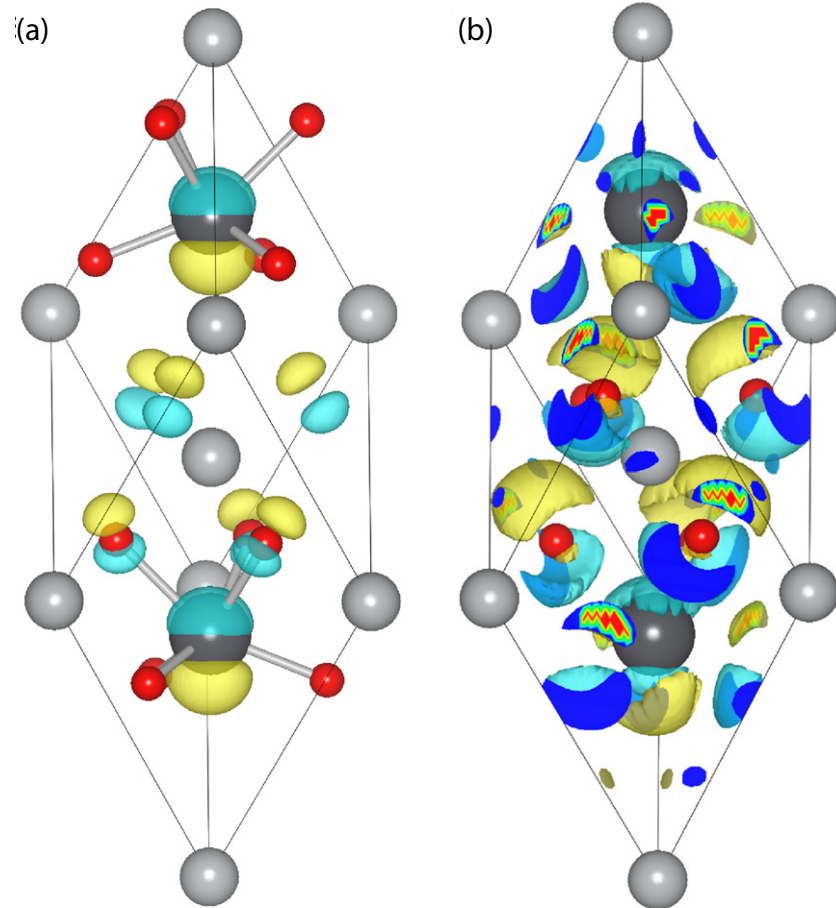


Figure 5. The difference in the PbNiO_3 calculated charge density (a) and electron localization function (ELF) (b) between the ferroelectric and the paraelectric phase within the HSE scheme. Yellow/blue regions correspond to an excess/depletion of charge and where electrons localize/delocalize. The black (large), gray (medium) and red (small) spheres denote Pb, Ni and O atoms, respectively. Only the distortion of the octahedron at the Pb site is shown.

the distortion further strengthens the covalent bonding between Pb 6s and O 2p orbitals along the [111]-direction.

Charge density difference analysis. In figure 5(a) we plot the charge density difference $\Delta\rho(\mathbf{r}) = \rho_{\text{ferro}}(\mathbf{r}) - \rho_{\text{para}}(\mathbf{r})$ between the ferroelectric $R3c$ and paraelectric $R-3c$ state.

In the paraelectric phase the electron density contour is symmetric along the [111]-direction, while in the ferroelectric phase the lack of the inversion center allows shifts of Pb and O atoms along the [111]-direction, giving rise to an asymmetric distribution of the electron density. As shown in figure 5(a), the difference of charge density contours clearly shows a strong asymmetric electron re-distribution around the Pb atoms along the [111]-direction in the ferroelectric phase. Again, this supports an asymmetric covalent bonding interaction between the Pb 6s and O 2p orbitals.

ELF analysis. We use the ELF analysis, which is a useful tool for describing the chemical bonding character in extended systems [94]. ELF is a measure of the probability of finding an electron near another same-spin electron. It is a ground state property and can be used to

discriminate between different kinds of bonding [94]. The ELF is represented as a contour plot in real space, spanning values between 0 and 1. A region where ELF is 1 means there is no possibility to find two electrons with the same spin. This usually occurs in regions occupied by bond pairs or lone pairs; ELF = 0 corresponds to vacuum, while in metals ELF \sim 0.5 [95]. In figure 5(b) we present the difference in ELF between the ferroelectric and paraelectric phases of PbNiO₃, i.e. $\Delta ELF(\mathbf{r}) = ELF_{\text{ferro}}(\mathbf{r}) - ELF_{\text{para}}(\mathbf{r})$. Thus, positive values of $\Delta ELF(\mathbf{r})$ represent the area where the electron localization is higher, i.e. the covalent bonding is strengthened; negative values of $\Delta ELF(\mathbf{r})$ represent the area where the electron localization is lower and the covalent bond weaker [90, 96].

The $\Delta ELF(\mathbf{r})$ isosurface clearly indicates that the ferroelectric distortion leads to a strongly asymmetric electron localization along the [111]-direction. The positive region mainly resides in the pyramid formed by the Pb atom and the three oxygen atoms above the Ni (0.5 0.5 0.5) atom; in contrast, the negative counterpart is predominately located in the pyramid formed by the Pb atom and the other three oxygen atoms beneath. This asymmetric distribution is associated with the asymmetric Pb and O atoms bonding interaction along the [111]-direction. The existence or absence of ferroelectricity is determined by a delicate balance between long-range Coulomb forces (which favor the ferroelectric state) and short-range repulsions which are minimized in the symmetric structure (favoring the non-polar paraelectric state [20]). The tendency of additional bonding between the Pb 6s and O 2p orbitals stabilizes the ferroelectric distortion.

All these results suggest that the asymmetric bonding interaction between the Pb 6s and O 2p orbitals due to the presence of the lone-pair on Pb is the primary driving force for ferroelectricity in rhombohedral PbNiO₃. Clearly, a naïve picture just based on the assumption of nominal charges is unable to capture this complexity.

3. Summary and conclusions

We have reported structural, electronic and magnetic properties for orthorhombic and rhombohedral PbNiO₃ obtained from *ab initio* density functional calculations using GGA, DFT+U and HSE. Besides providing a detailed analysis of the pressure-driven *R3c-Pnma* structural transition, we have re-explored and discussed the ferroelectric properties of rhombohedral PbNiO₃, which is characterized by a large spontaneous polarization, comparable to that of BiFeO₃. Density of states, Born effective charge, charge density and ELF analysis have been used to study the ferroelectric transition.

Our main conclusions are:

- (1) The calculated structural parameters for rhombohedral PbNiO₃ via the GGA+U and HSE scheme are in agreement with experimental values, especially for the HSE method, while GGA (PBE) fails to reproduce the relevant properties.
- (2) A pressure induced structural transition from the rhombohedral to the orthorhombic structure occurs around 5 GPa at the GGA+U level. This scenario is in agreement with experimental observations. On the other hand, the GGA (PBE) scheme predicts the orthorhombic phase to be the ground state, in sharp contrast with the experiments.
- (3) The study of the magnetic interactions reveals a significant anisotropy of the nearest-neighbor exchange couplings in the orthorhombic phase. This magnetic anisotropy is considerably attenuated (virtually vanishes) in the ferroelectric rhombohedral LiNbO₃-type phase. The computed magnetic transition temperature is in line with the measured one.

- (4) Detailed analysis of the density of states indicates that the valence state of the Pb ions is smaller than the nominal charge 4+, in contrast to naïve expectations based on the fact that Ni is found to be in a high spin 2+ state.
- (5) Our study confirms that rhombohedral PbNiO_3 might be a potential candidate for multiferroic applications. The spontaneous polarization is $100 \mu\text{C cm}^{-2}$ along the [111]-direction, comparable to that of BiFeO_3 .
- (6) The asymmetric hybridization interaction between Pb 6s and O 2p orbitals appears as the driving force of atomic polar displacements along the [111]-direction, thus giving rise to a large spontaneous polarization.

Acknowledgments

Work supported in part by the European Union FP7 program and Department of Science and Technology of India under the joint EU–India project ‘ATHENA’ (grant agreement no. 233553). Supercomputer time in Austria was provided by the Vienna Scientific Cluster. Figures were prepared using the VESTA package [97]. XH gratefully acknowledges Clauder Ederer and Chung-Yuan Ren for helpful advices and comments. AS would like to thank Professor A Sayede for the kind invitation at Université d’Artois, Faculté des Sciences Jean Perrin where this work was finalized. AF and SP acknowledge MIUR-PRIN 2010 *Oxide*. AF also acknowledges IIT-Seed NEWDFESCM, IIT-SEED POLYPHEMO and ‘platform computation’ of IIT, and Fondazione Banco di Sardegna grants. AS, PB and SP acknowledge support from the PRACE initiative at CINECA (IT) and Barcelona Supercomputing Centers (ES) and from CARIPLO Foundation through the ECOMAG project (no. 2010-0584).

References

- [1] Ziese M and Thornton M J (ed) 2001 *Spin Electronics (Lecture Notes in Physics vol 569)* (Berlin: Springer)
- [2] Scott J F 2000 *Ferroelectric Memories (Series in Advanced Microelectronics vol 3)* (Berlin: Springer)
- [3] Rabe K M, Ahn C H and Triscone J M (ed) 2007 *Physics of Ferroelectrics: A Modern Perspective (Topics in Applied Physics vol 105)* (Berlin: Springer)
- [4] Schmid H 1973 *Int. J. Magn.* **4** 337–61
- [5] Khomskii D I 2009 *Physics* **2** 20
- [6] Wang K F, Liu J M and Ren Z F 2009 *Adv. Phys.* **58** 321
- [7] Pyatakov A P and Zvezdin A K 2012 *Phys.—Usp.* **55** 557–81
- [8] Cheong S W and Mostovoy M 2007 *Nature Mater.* **6** 13
- [9] Tokura Y and Seki S 2010 *Adv. Mater.* **22** 1554
- [10] Ramesh R and Spaldin N A 2007 *Nature Mater.* **6** 21
- [11] King-Smith R D and Vanderbilt D 1993 *Phys. Rev. B* **47** 1651–4
- [12] Vanderbilt D and King-Smith R D 1993 *Phys. Rev. B* **48** 4442–55
- [13] Resta R 1994 *Rev. Mod. Phys.* **66** 899–915
- [14] Picozzi S and Stroppa A 2012 *Eur. Phys. J. B* **85** 240
- [15] Picozzi S and Ederer C 2009 *J. Phys.: Condens. Matter* **21** 303201
- [16] Stroppa A and Picozzi S 2010 *Phys. Chem. Chem. Phys.* **12** 5405–16
- [17] Matthias B T 1949 *Phys. Rev.* **75** 1771
- [18] Bersuker I 1966 *Phys. Lett.* **20** 589–90
- [19] Lines M E and Glass A M (ed) 1977 *Principles and Applications of Ferroelectrics and Related Materials* (Oxford: Clarendon)

- [20] Cohen R E 1992 *Nature* **358** 136–8
- [21] Hill N A 2000 *J. Phys. Chem. B* **104** 6694
- [22] Filippetti A and Hill N A 2002 *Phys. Rev. B* **65** 195120
- [23] Bersuker I B 2012 *Phys. Rev. Lett.* **108** 137202
- [24] Bhattacharjee S, Bousquet E and Ghosez P 2009 *Phys. Rev. Lett.* **102** 117602
- [25] Rondinelli J M, Eidelson A S and Spaldin N A 2009 *Phys. Rev. B* **79** 205119
- [26] Barone P, Kanungo S, Picozzi S and Saha-Dasgupta T 2011 *Phys. Rev. B* **84** 134101
- [27] Günter T, Bousquet E, David A, Boullay P, Ghosez P, Prellier W and Fiebig M 2012 *Phys. Rev. B* **85** 214120
- [28] Sakai H *et al* 2011 *Phys. Rev. Lett.* **107** 137601
- [29] Lee J H and Rabe K M 2010 *Phys. Rev. Lett.* **104** 207204
- [30] Giovannetti G, Kumar S, Ortix C, Capone M and van den Brink J 2012 *Phys. Rev. Lett.* **109** 107601
- [31] Xu Y, Hao X, Franchini C and Gao F 2013 *J. Phys. Chem. C* submitted
- [32] Rondinelli J M and Fennie C J 2012 *Adv. Mater.* **24** 1961–8
- [33] Benedek N A and Fennie C J 2013 *J. Phys. Chem. C* **117** 13339–49
- [34] Singh D J and Park C H 2008 *Phys. Rev. Lett.* **100** 087601
- [35] Bousquet E, Dawber M, Stucki N, Lichtensteiger C, Hermet P, Gariglio S, Triscone J M and Ghosez P 2008 *Nature* **452** 732
- [36] Fukushima T, Stroppa A, Picozzi S and Perez-Mato J M 2011 *Phys. Chem. Chem. Phys.* **13** 12186
- [37] Benedek N A and Fennie C J 2011 *Phys. Rev. Lett.* **106** 107204
- [38] López-Pérez J and Íñiguez J 2011 *Phys. Rev. B* **84** 075121
- [39] Scarrozza M, Filippetti A and Fiorentini V 2012 *Phys. Rev. Lett.* **109** 217202
- [40] Scarrozza M, Filippetti A and Fiorentini V 2013 *Eur. Phys. J. B* **86** 128
- [41] Ghita M, Fornari M, Singh D J and Halilov S V 2005 *Phys. Rev. B* **72** 054114
- [42] Kan E, Xiang H, Lee C, Wu F, Yang Y and Whangbo M H 2010 *Angew. Chem. Int. Edn Engl.* **49** 1603–6
- [43] Stroppa A, Jain P, Barone P, Marsman M, Perez-Mato J M, Cheetham A K, Kroto H W and Picozzi S 2011 *Angew. Chem. Int. Edn Engl.* **50** 5487
- [44] Stroppa A, Barone P, Jain P, Perez-Mato J M and Picozzi S 2013 *Adv. Mater.* **25** 2284
- [45] Seshadri R and Hill N 2001 *Chem. Mater.* **13** 2892
- [46] Neaton J B, Ederer C, Waghmare U V, Spaldin N A and Rabe K M 2005 *Phys. Rev. B* **71** 014113
- [47] Goffinet M, Hermet P, Bilc D I and Ghosez P 2009 *Phys. Rev. B* **79** 014403
- [48] Diéguez O, Aguado-Puente P, Junquera J and Íñiguez J 2013 *Phys. Rev. B* **87** 024102
- [49] Escorihuela-Sayalero C, Diéguez O and Íñiguez J 2012 *Phys. Rev. Lett.* **109** 247202
- [50] Lebeugle D, Colson D, Forget A and Viret M 2007 *Appl. Phys. Lett.* **91** 022907
- [51] Kadomtseva A M, Zvezdin A, Popov Y F, Pyatakov A P and Vorob'ev G P 2004 *JETP Lett.* **79** 571
- [52] Park J *et al* 2011 *J. Phys. Soc. Japan* **80** 114714
- [53] Johnson R D, Barone P, Bombardi A, Bean R J, Picozzi S, Radaelli P G, Oh Y S, Cheong S W and Chapon L C 2013 *Phys. Rev. Lett.* **110** 217206
- [54] Tokunaga M, Azuma M and Shimakawa Y 2010 *J. Phys. Soc. Japan* **79** 064713
- [55] Baettig P, Seshadri R and Spaldin N 2007 *J. Am. Chem. Soc.* **129** 9854
- [56] Belik A A *et al* 2007 *J. Am. Chem. Soc.* **129** 971–7
- [57] Solovyev I V and Pchelkina Z V 2010 *Phys. Rev. B* **82** 094425
- [58] Imada M, Fujimori A and Tokura Y 1998 *Rev. Mod. Phys.* **70** 1039–263
- [59] Lee P A, Nagaosa N and Wen X G 2006 *Rev. Mod. Phys.* **78** 17–85
- [60] Woodward P M 1997 *Acta. Cryst. B* **53** 32–43
- [61] Bersuker I B 2006 *The Jahn-Teller Effect* (Cambridge: Cambridge University Press)
- [62] Goldschmidt V M 1926 *Die Naturwissenschaften* **21** 477–85
- [63] Inaguma Y, Tanaka K, Tsuchiya T, Mori D, Katsumata T, Ohba T, Hiraki K, Takahashi T and Saitoh H 2011 *J. Am. Chem. Soc.* **133** 16920–9
- [64] Inaguma Y, Yoshida M, Tsuchiya T, Aimi A, Tanaka K, Katsumata T and Mori D 2010 *J. Phys.: Conf. Ser.* **215** 012131

- [65] Hao X F, Stroppa A, Picozzi S, Filippetti A and Franchini C 2012 *Phys. Rev. B* **86** 014116
- [66] Xu Y, Hao X, Franchini C and Gao F 2013 *Inorg. Chem.* **52** 1032–9
- [67] Kresse G and Hafner J 1993 *Phys. Rev. B* **48** 13115–8
- [68] Blöchl P 1994 *Phys. Rev. B* **50** 17953–79
- [69] Elsässer C, Fähnle M, Chan C T and Ho K M 1994 *Phys. Rev. B* **49** 13975–8
- [70] Monkhorst H J and Pack J D 1976 *Phys. Rev. B* **13** 5188–92
- [71] Perdew J P, Burke K and Ernzerhof M 1996 *Phys. Rev. Lett.* **77** 3865–8
- [72] Anisimov V I, Solovyev I V, Korotin M A, Czyzyk M T and Sawatzky G A 1993 *Phys. Rev. B* **48** 16929–34
- [73] Solovyev I V, Dederichs P H and Anisimov V I 1994 *Phys. Rev. B* **50** 16861–71
- [74] Cococcioni M and de Gironcoli S 2005 *Phys. Rev. B* **71** 035105
- [75] Kornev I A, Lisenkov S, Haumont R, Dkhil B and Bellaiche L 2007 *Phys. Rev. Lett.* **99** 227602
- [76] Solovyev I, Hamada N and Terakura K 1996 *Phys. Rev. B* **53** 7158–70
- [77] Anisimov V I, Aryasetiawan F and Liechtenstein A I 1997 *J. Phys.: Condens. Matter* **9** 767–808
- [78] Terakura K, Oguchi T, Williams A R and Kübler J 1984 *Phys. Rev. B* **30** 4734–47
- [79] Dudarev S L, Botton G A, Savrasov S Y, Humphreys C J and Sutton A P 1998 *Phys. Rev. B* **57** 1505–9
- [80] Heyd J, Scuseria G and Ernzerhof M 2003 *J. Chem. Phys.* **118** 8207–15
- [81] He J and Franchini C 2012 *Phys. Rev. B* **86** 235117
- [82] Di Sante D, Barone P, Bertacco R and Picozzi S 2013 *Adv. Mater.* **25** 509
- [83] Wahl R, Vogtenhuber D and Kresse G 2008 *Phys. Rev. B* **78** 104116
- [84] Di Sante D, Stroppa A and Picozzi S 2012 *Phys. Chem. Chem. Phys.* **14** 14673
- [85] Franchini C, Archer T, He J, Chen X Q, Filippetti A and Sanvito S 2011 *Phys. Rev. B* **83** 220402
- [86] Togo A, Oba F and Tanaka I 2008 *Phys. Rev. B* **78** 134106
- [87] Archer T *et al* 2011 *Phys. Rev. B* **84** 115114
- [88] Solovyev I V and Terakura K 1998 *Phys. Rev. B* **58** 15496–507
- [89] Teague J R, Gerson R and James W J 1970 *Solid State Commun.* **8** 1073–4
- [90] Stroppa A, Marsman M, Kresse G and Picozzi S 2010 *New J. Phys.* **12** 093026
- [91] Veithen M and Ghosez P 2002 *Phys. Rev. B* **65** 214302
- [92] Nakayama M, Nogami M, Yoshida M, Katsumata T and Inaguma Y 2010 *Adv. Mater.* **22** 2579–82
- [93] Ravindran P, Vidya R, Kjekshus A, Fjellvåg H and Eriksson O 2006 *Phys. Rev. B* **74** 224412
- [94] Savin A, Nesper R, Wengert S and Fässler T F 1997 *Angew. Chem. Int., Edn Engl.* **36** 1808–32
- [95] Becke A D and Edgecombe K E 1990 *J. Chem. Phys.* **92** 5397–403
- [96] Oak M A, Lee J H, Jang H M, Goh J S, Choi H J and Scott J F 2011 *Phys. Rev. Lett.* **106** 047601
- [97] Momma K and Izumi F 2008 *J. Appl. Crystallogr.* **41** 653–8